THE EUROPEAN
PHYSICAL JOURNAL PLUS

Taguchi optimization of integrated flow microfluidic biosensor for COVID-19 detection

Sameh Kaziz[1,2,a] , **Ibrahim Ben Mariem**[1], **Fraj Echouchene**[3,4], **Maissa Belkhiria**[3], **Hafedh Belmabrouk**[5]

[1] Quantum and Statistical Physics Laboratory, Faculty of Sciences of Monastir, University of Monastir, Environment Boulevard, 5019 Monastir, Tunisia
[2] Higher National Engineering School of Tunis, Taha Hussein Montfleury Boulevard, University of Tunis, 1008 Tunis, Tunisia
[3] Laboratory of Electronics and Microelectronics, Faculty of Science of Monastir, University of Monastir, Environment Boulevard, 5019 Monastir, Tunisia
[4] Higher Institute of Applied Sciences and Technology of Sousse, University of Sousse, Sousse, Tunisia
[5] Department of Physics, College of Science at Zulfi, Majmaah University, Al Majma'ah, Saudi Arabia

Abstract In this research, Taguchi's method was employed to optimize the performance of a microfluidic biosensor with an integrated flow confinement for rapid detection of the SARS-CoV-2. The finite element method was used to solve the physical model which has been first validated by comparison with experimental results. The novelty of this study is the use of the Taguchi approach in the optimization analysis. An $L8(2^7)$ orthogonal array of seven critical parameters—Reynolds number (Re), Damköhler number (Da), relative adsorption capacity (σ), equilibrium dissociation constant (K_D), Schmidt number (Sc), confinement coefficient (α) and dimensionless confinement position (X), with two levels was designed. Analysis of variance (ANOVA) methods are also used to calculate the contribution of each parameter. The optimal combination of these key parameters was Re $= 10^{-2}$, Da $= 1000$, $\sigma = 0.5$, $K_D = 5$, Sc $= 10^5$, $\alpha = 2$ and X $= 2$ to achieve the lowest dimensionless response time (0.11). Among the all-optimization factors, the relative adsorption capacity (σ) has the highest contribution (37%) to the reduction of the response time, while the Schmidt number (Sc) has the lowest contribution (7%).

1 Introduction

Since the emergence of the COVID-19 pandemic caused by the novel coronavirus, i.e., severe acute respiratory syndrome coronavirus-2 (SARS-CoV-2), at the end of December 2019 in Wuhan, China [1], researchers have not stopped searching for innovative approaches to detect infections as quickly as possible, reliably, and sensitively in order to control and limit the rapid spread of the disease. Among these approaches, microfluidic biosensors have taken a prominent place in the identification of SARS-CoV-2 and thus in the fight against the pandemic [2, 3]. A microfluidic biosensor is an analytical tool composed of a bioreceptor element, which can be an antibody, an enzyme, a DNA fragment, or a whole cell, which allows the identification of the species to be detected due to its particularly selective site. The bioreceptor is linked to a transducer element capable of converting biological information into an electrical signal—a physical, mechanical, thermal, or optical one [4, 5]. The characteristics and performance of these biosensor devices are strongly linked to sensitivity, specificity, reliability, simplicity, low cost and especially to the rapid detection.

Currently, diagnostic techniques for patients with SARS-CoV-2 are the quantitative real-time polymerase chain reaction (qRT-PCR), CT scans, antigenic tests, serological tests, etc. Although qRT-PCR is the most widely used detection method for detecting COVID-19 [6, 7], it requires complex equipment and skilled operators. It is also slow, expensive, and laborious [8, 9]. Point-of-care (POC) biosensors that are also used for rapid diagnosis of COVID-19 disease are polydimethylsiloxane (PDMS) chip-based biosensors or paper-based biosensors, like lateral flow test strips [10, 11]. These tests are generally used to detect antigens, antibodies, or nucleic acids in raw samples (sputum, saliva, and blood) [12]. Antibody tests are appropriate for detecting late-stage infections, whereas nucleic acid tests identify the presence of nucleic acids (viruses) at an early phase of infection, revealing sensitivity and specificity superior to antibody tests. Nevertheless, nucleic acid testing requires more complicated processes than antibody testing such as nucleic acid extraction, amplification, and detection [13]. Compared to existing POC biosensors, qRT-PCR shows higher clinical sensitivity and specificity.

To enhance functionality and detection sensitivity of current biosensors, many numerical and experimental studies have been made. Magnetic effect [14], electrokinetic effect [15–18], optical forces [19], etc., are physical mechanisms that have been applied to agitate the flows in the microchannel to increase the rate of the biosensor binding reaction. Selmi et al. [20, 21] simulated the effect of confining flow (flux injection), added perpendicular to the main flow, to reduce the diffusion layer and improve biosensor

[a] e-mail: kaziz_sameh@yahoo.fr (corresponding author)

Springer

performance. Also, the adjustment of certain key parameters of microfluidic biosensors was one of the means used to optimize the detection time of these devices. Kaziz et al. [18] performed a 3D study on the effect of reaction surface shape on the response time of microfluidic biosensor with electrothermal force. The obtained results are compared to the same biosensor having a rectangular binding surface [17]. Shahbazi et al. [22] showed that the impact of moving the reaction surface position by just 500 μm decreased the saturation time by further than 50%.

In this article, a 2D finite element simulation on the binding kinetics of SARS-CoV-2 was performed to optimize the performance of the flow-confinement microfluidic biosensor. To determine the degree of influence of some input factors on the detection time, Taguchi's numerical plan of experiment, based on analysis of variance (ANOVA) and mean effect, was adopted as a support for the modeling of the microfluidic biosensor, in order to have the minimum number of simulations to be performed. Design of experiments (DOE) is a methodology for determining the links between process input variables and a quantity of interest, called the response. The variables, physical quantities modifiable by the experimenter, are supposed to influence the variations of the response. Using the plans of experiments, one obtains the maximum of information with the minimum of experiments [23]. A full factorial experiment takes all possible combinations of each key parameter to study their effects on the response variable. If there are n parameters with 2 levels each, then the full-factor design has 2^n tests. This large number of experiments is costly in terms of time and energy. To overcome this problem, Taguchi introduced an experiment design technique using an orthogonal array (OA) to study the whole range of factors with a reduced number of experiments [24]. Therefore, the time as well as the cost is significantly reduced. ANOVA is then used to determine the significance and contribution of each process parameter to the output characteristic. With main effects and ANOVA analyses, a possible combination of optimal parameters can be predicted. Finally, a confirmation experiment is conducted to verify the obtained optimal process parameters.

The Taguchi approach is utilized in several domains like physics [25], medicine [26], environmental sciences [27, 28], chemical processes [29] and statistics [30]. ANOVA is one of the most common techniques used to do statistical analysis of data [31].

2 Mathematical model

2.1 Confined flow microfluidic biosensor design

Figure 1 shows the design model of the confined flow microfluidic biosensor investigated in this study. The length "L" and the height "H" of the microchannel are 250 μm and 40 μm, respectively.

The reaction surface, of length is $l_s = 20$ μm, is placed on the microchannel bottom. On the upper wall of the microchannel, a flow confinement, perpendicular to the main flow, is situated at a distance X from the entrance of the microchannel.

The carrier fluid, which is water, mixed with the analytes (SARS-CoV-2) flows in the microchannel from left to right. Ligands (antibodies) of constant concentration are initially immobilized on the reaction surface.

2.2 Modeling of Navier–Stokes equations

For incompressible fluid, the Navier–Stokes equations describing the flow of the carrier fluid in the microchannel were considered in terms of dimensionless amounts [32] as follows (Eq. (1) and Eq. (2)):

$$\nabla^* . \overrightarrow{U^*} = 0 \tag{1}$$

$$\overrightarrow{U^*} . (\nabla^* \overrightarrow{U^*}) = -\nabla^* p^* + \frac{1}{Re} \Delta^* \overrightarrow{U^*} \tag{2}$$

All the variables used in the Navier–Stokes equations are dimensionless. The quantities without and with asterisk designate, respectively, dimensional and dimensionless variables. $Re = \frac{\rho u_0 H}{\mu}$ represents the Reynolds number where ρ and μ are, respectively, the fluid's density and dynamic viscosity, u_0 is the average inlet velocity, and H is the microchannel height. The dimensionless components of the velocity vector are $u^* = \frac{u}{u_0}$ and $v^* = \frac{v}{u_0}$. The confinement coefficient, α, is identified as the velocity confinement ratio of the stream to that of the mainstream containing the target analytes ($\alpha = \frac{U_{conf}}{u_0}$). H, u_0 and ρu_0^2 are the length, the velocity, and the pressure scales, respectively.

2.3 Modeling of the analyte transport equation

The combination of convection and diffusion effects within the microchannel contributes to concentration gradients. The convection–diffusion equation [20] describing the spatio-temporal evolution of analyte concentration in the fluid inside the microchannel is expressed by (Eq. (3)):

$$\frac{\partial C^*}{\partial t^*} + \text{Pe} \overrightarrow{U^*} \cdot \nabla^* C^* = \Delta^* C^* \tag{3}$$
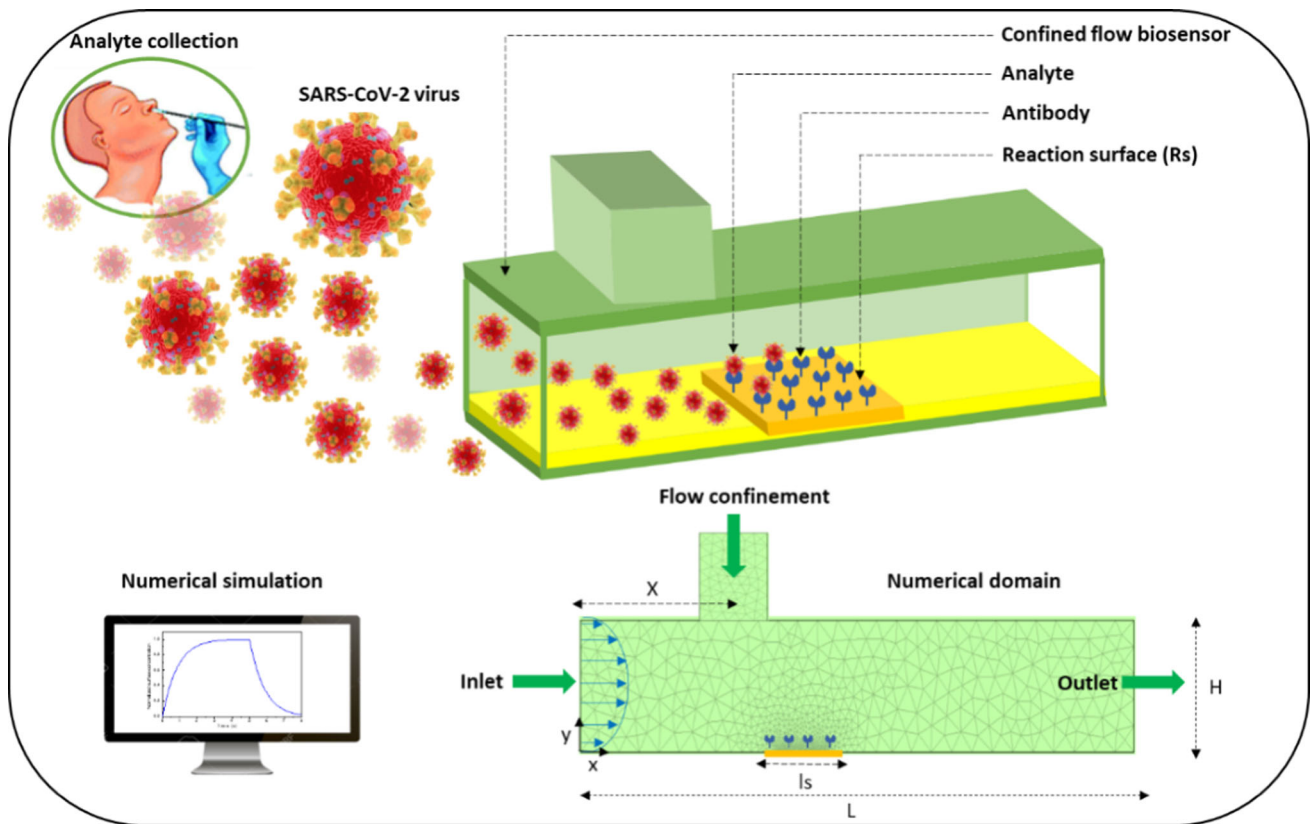
Fig. 1 Sketch of the confined flow microfluidic biosensor

where $C^* = \frac{C}{C_0}$ is the dimensionless concentration of the analyte, and $t^* = \frac{t}{t_0}$ is the dimensionless time. C_0 is the inlet analyte concentration, $\frac{\partial C^*}{\partial t^*}$ is the dimensionless concentration gradient, $Pe = \frac{u_0 H}{D}$ is the Peclet number. The time scale is $t_0 = \frac{H^2}{D}$, and the concentration scale is C_0. In the context of mass transport, the Peclet number is the product of the Schmidt number (Sc) and the Reynolds number.

2.4 Modeling of the kinetic analyte–ligand reaction

The first-order Langmuir–Hinshelwood adsorption model [33, 34] (Eq. (4)) was employed to calculate the analyte–ligand complex concentration formed on the reaction surface.

$$\frac{\partial B^*}{\partial t^*} = Da.\sigma \left[C^*_{surf}(1 - B^*) - \frac{1}{K_A C_0} B^* \right] \tag{4}$$

where $B^* = \frac{B}{B_{max}}$, B is the bound complex concentration, and B_{max} is the initial concentration of ligand immobilized on the binding surface. $C^*_{surf} = \frac{C_{surf}}{C_0}$ where C_{surf} is the analyte concentration at the reaction surface, $Da = \frac{K_{on} B_{max} H}{D}$ is the Damköhler number, $\sigma = \frac{H C_0}{B_{max}}$ is the relative adsorption capacity, and $K_A = \frac{k_{on}}{k_{off}}$ is the affinity constant where k_{on} and k_{off} are the adsorption and the desorption constants, respectively. $\boldsymbol{K_D} = \frac{1}{K_A C_0}$ is the dimensionless equilibrium dissociation constant.

The relative adsorption capacity (σ) corresponds to the relative density of analytes between the bulk and the fully saturated surfaces (a measure of surface adsorption capacity relative to the bulk). It occurs when matching the units of surface concentration and bulk concentration [35, 36]. The Damkohler number (Da) is used in chemical kinetics to define the operating conditions of a reaction. If Da < < 1, the reaction is very slow and if Da > > 1, the reaction is very fast, and the flow is in chemical equilibrium.

3 Initial and boundary conditions

Initially, the dimensionless fluid velocity (U^*) is assumed equal to unity. Also, the concentration of analyte, $C_{(t=0)}$, and the surface complex analyte/ligand concentration, $B_{(t=0)}$, were initially zero. All boundary conditions for velocity and analyte concentration used in this model are summarized in Fig. 2 where $\overrightarrow{n}$ is the unit normal vector to the surface. For the fluid flow mode, the non-slip

Fig. 2 Boundary conditions. **a**: Velocity field boundary conditions. **b**: Analyte concentration boundary conditions
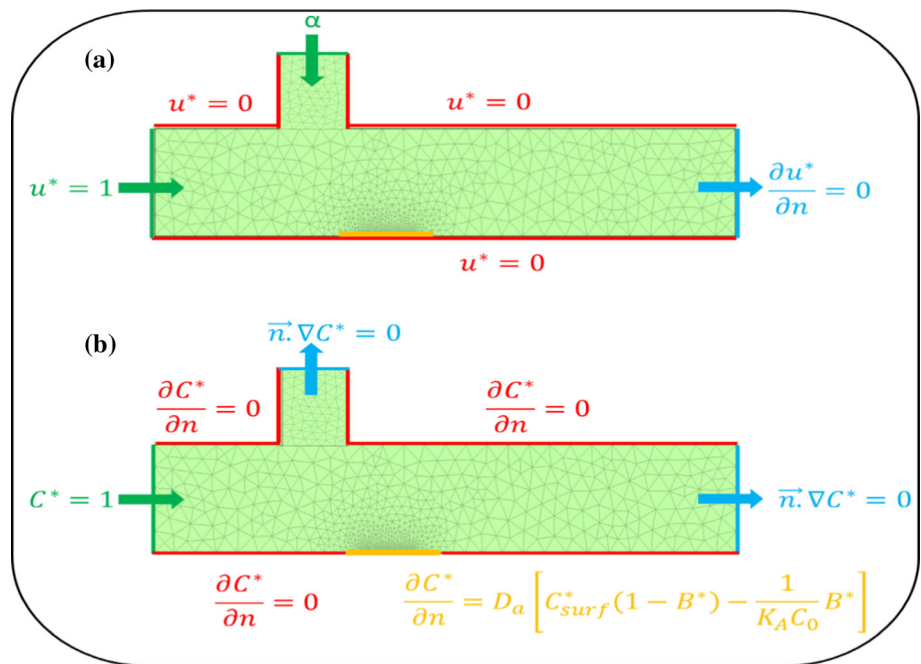
Table 1 Simulation parameters

Parameter	Description	Value	Unit
ρ	Fluid density	1000	kg/m^3
μ	Dynamic viscosity	$1{,}08.10^{-3}$	Pa.s
K_A	Affinity constant	10^6	m^3/Mol
B_{max}	Ligand concentration	$3{,}3.10^{-8}$	Mol/m^2
L	Microchannel length	250	µm
H	Microchannel height	40	µm
ls	Reaction surface length	20	µm

conditions along the walls of the microfluidic device are applied, a parabolic velocity distribution with average value u_0 is given to the carrier fluid at the inlet of the microchannel, the one entering through the confining channel, its velocity was set to u_{conf} and at the outlet the flow is assumed fully developed. For the transport equation (Eq. (3)), a low concentration of analyte C_0 is injected at the inlet, and the convective flow condition is applied at the outlet. On the sensitive surface, the diffusive flux condition generated by the binding reaction between analytes and ligands is applied and the homogeneous Neumann condition is used for the other walls because they are assumed to be impermeable and do not interact with the target analyte [22].

To evaluate the influence of control parameters on SARS-CoV-2 binding kinetics, we performed numerical simulations using the geometric design of the microfluidic biosensor proposed in Fig. 1. The geometric dimensions, the fluid physical parameters and SARS-CoV-2/Antibody binding factors [22] used for the simulation are shown in Table 1.

4 Parameters and levels selection

In this study, different controllable parameters were selected to be optimized, in order to maximize the efficiency of the biosensor. The Reynolds number Re, the Damkohler number Da, the relative adsorption capacity σ, the equilibrium dissociation constant K_D, the Schmidt number Sc, the confinement coefficient α and the confinement position X are the seven variables that we have considered to optimize by the Taguchi method in order to obtain their optimal combination giving the shortest detection time.

4.1 Reynolds number

In microfluidic devices, flow velocities are typically low (a few tenths of a millimeter per second), resulting in a low Reynolds number [20]. As the carrier fluid in our case is water ($\rho = 10^3$kg.m^{-3}, $\mu = 1,08.10^{-3}$) Pa.s, then the Reynolds number varies between 10^{-3} and 10^{-2} for flow velocities varying between 10^{-4} and 10^{-3} m.s^{-1}.

4.2 Damkohler number

When we fix the surface concentration of binding sites on the biosensor ($B_{max} = 3, 3.10^{-8} \text{Mol.m}^{-2}$) [16–18, 22] and the height of the microchannel ($H = 40.10^{-6}$m), the Damkohler number becomes dependent only on the diffusion coefficient of the target analyte (D) and the adsorption analyte-antibody constant (K_{on}). As the diffusion coefficient can vary from 10^{-11} to 10^{-10} m^2. s^{-1} and the adsorption constant between 10^2 and 10^4 m^3/Mol.s for SARS-CoV-2 [22], then the Damkohler number can vary between 1 and 1000.

4.3 Relative adsorption capacity

For low concentrations of target analyte (of the order of 10^{-5} Mol/m^3 and 10^{-4} Mol/m^3), the relative adsorption capacity can vary from 10^{-2} to 10^{-1} with the same values of B_{max} and H. For high relative adsorption capacity (low σ), the bulk concentration reaches a steady-state value much before the surface has been significantly saturated [35].

4.4 Schmidt number

As the Schmidt number, which is the ratio of the Peclet number to the Reynolds number ($Sc = \frac{Pe}{Re}$), is inversely proportional to the antigen diffusion coefficient (D), for a given density and dynamic viscosity of the carrier fluid, then it can vary between 10^4 and 10^5 for the same range of variation of D indicated before.

5 Model simulation

The proposed model equations were solved using Galerkin finite element analysis [37]. 1549 triangular geometric elements were used for the whole 2D domain including the refined elements of the reaction surface. First, the pressure and velocity fields were calculated by simultaneously solving stationary Eqs. (1) and (2). The analyte and complex concentrations were simulated from the coupled time-dependent Eqs. (3) and (4). In the numerical model, the reaction surface is taken into account as a boundary condition where the diffusion flux is balanced against the reaction rate. The average complex concentration $\langle B^* \rangle$ at the reaction surface is calculated by this equation (Eq. (5)):

$$\langle B^* \rangle = \frac{1}{l_s^*} \int_0^{l_s^*} B(x) dx \tag{5}$$

where $l_s^* = \frac{l_s}{H}$ is the dimensionless length of the binding surface.

The response time corresponds to the time for which the concentration of the complex is 95% is extracted from the time evolution of $\langle B^* \rangle$.

6 Experimental design

The experiment using Taguchi method was considered in this numerical simulation to decrease the response time of the integrated flow confinement microfluidic biosensor. Table 2 shows seven optimization parameters having two levels each used in the experiment design. If there are seven factors called A, B, C, D, E, F and G, all are examined with two levels called "1" and "2." A full factorial design requires $2^7 = 128$ combinations. In order to reduce this number, the orthogonal array of $L_8(2^7)$, based on the Taguchi method, was used and is represented in Table 3. This design requires eight experiments with seven simulation parameters at two levels of each neglecting the interactions between them.

Table 2 Levels of control parameters	Symbol	Control parameter	Level 1	Level 2
	Re	Reynolds number	5.10^{-3}	10^{-2}
	Da	Damköhler number	5	1000
	σ	Relative adsorption capacity	0.02	0.5
	K_D	Equilibrium dissociation constant	1	5
	Sc	Schmidt number	10^4	10^5
	α	Confinement coefficient	0.1	2
	X	Dimensionless confinement position	0.5	2

Table 3 Taguchi's $L_8(2^7)$ orthogonal array

Standard Order	Factors						
	Re	Da	σ	K_D	Sc	α	X
1	1	1	1	1	1	1	1
2	1	1	1	2	2	2	2
3	1	2	2	1	1	2	2
4	1	2	2	2	2	1	1
5	2	1	2	1	2	1	2
6	2	1	2	2	1	2	1
7	2	2	1	1	2	2	1
8	2	2	1	2	1	1	2

Fig. 3 Comparison of our model with the experimental results of Hoffman et al.[33]
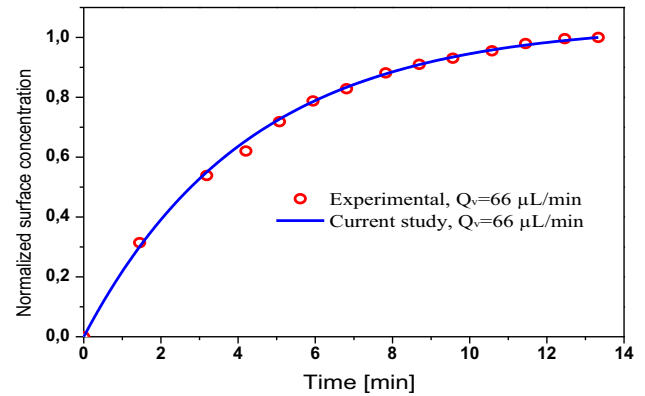
7 Results and discussion

7.1 Model validation

First, the numerical model was tested by comparison with experimental existing data of Hofmann et al. [33], as shown in Fig. 3. The time-normalized surface concentration during the adsorption phase was calculated using the same experimental parameters used for the immunoassay concerning the rabbit Immunoglobulin G (IgG) and Cy-5-labeled anti-rabbit IgG in a microchannel with confinement effect. Validation is performed for small concentration of analyte ($c_0 = 10 \, \mu$mol/m^3) mixed with buffer fluid (water) flowing through a 3D dimensional microfluidic channel of dimensions 25 mm × 5 mm × 0.02 mm with a flow rate Qv = 66 μL/min. A circular detection area with a diameter of 4 mm is fixed in the lower microchannel wall. The analyte is characterized by a diffusion coefficient of 3×10^{-11} m^2/s. The surface concentration of the antibody ligand, dissociation and association rate of the biosensor is 2.387×10^{-7} mol/m^2, 3.5×10^{-3} s^{-1} and 240 m^3/mol·s, respectively.

We can note that the average error between the two results is very small which makes it possible to consider that the model is proven, and that it can be used for other topics.

7.2 The diffusion boundary layer thickness

The size of SARS-CoV-2 is on the order of 100 nm, so the binding reaction is expected to be strongly restricted by mass transport [38] owing to the low diffusion coefficient and the high affinity for a virus of such large size. The limited mass transport generally causes the development of a diffusion boundary layer above the reaction surface which thickness is written as follows [39] (Eq. (6)):

$$d_{diff} = \frac{1}{0.98}\left(\frac{DHl}{u}\right)^{1/3}$$ (6)

where u is the flow velocity, D is the diffusion constant of the analyte, H is the channel height, and l is the position along the binding surface. In dimensionless notation, d_{diff}^* factor is written as below (Eq. (7)):

$$d_{\text{diff}}^* = \frac{1}{0.98}\left(\frac{l^*}{P_e \, u^*}\right)^{1/3}$$ (7)

where $l^* = \frac{l}{H}$, $P_e = R_e.Sc = \frac{u_0 H}{D}$ is the Peclet number and $u^* = \frac{u}{u_0}$.

Fig. 4 Diffusion boundary layers as a function of the dimensionless position (X) of the confining flow. **a**: $X = 0.5$ and **b**: $X = 2$. (R_S is the reaction surface)
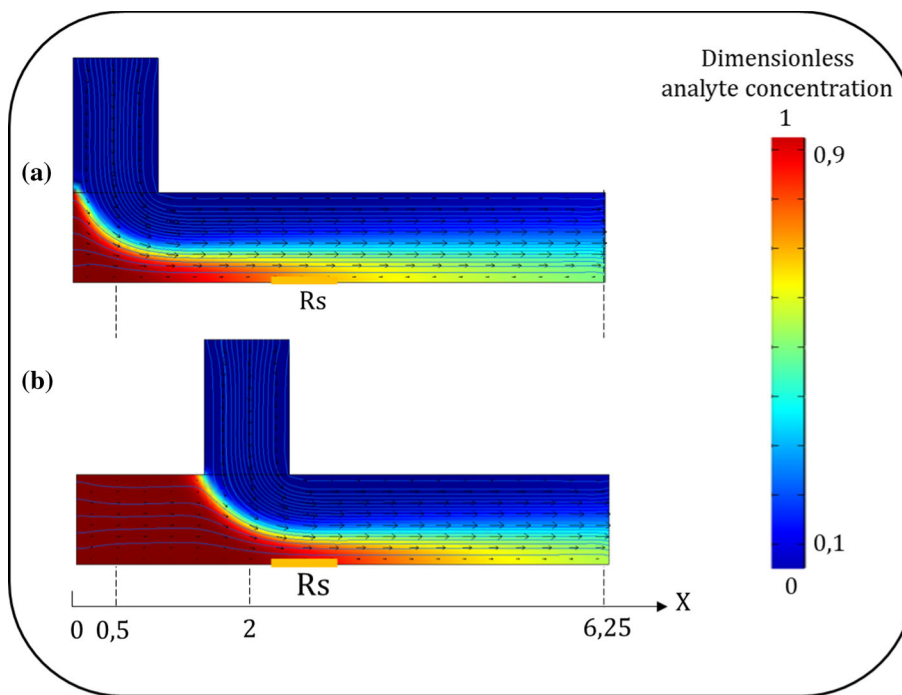
Fig. 5 Diffusion boundary layer thickness as a function of Reynolds number and position along the sensing zone
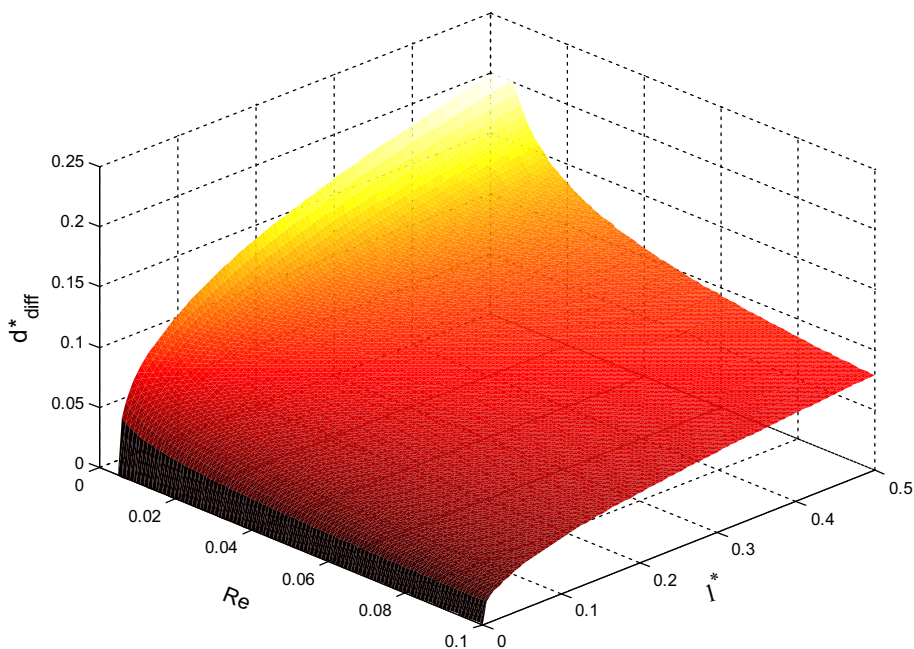

Figure 4 reveals the diffusion boundary layers for the two dimensionless positions of the confinement flow, namely $X = 0.5$ and $X = 2$, for the same confinement coefficient ($\alpha = 2$). As expected, the diffusion boundary layer seems thinner in the case where the confinement of the flow is located roughly opposite the reaction surface because it contributes better to pushing the analytes toward the sensitive surface as evidenced by the shape of the velocity arrows and streamlines plotted in Fig. 4.

Figure 5 shows the variation of the dimensionless of the diffusion layer as a function of the dimensionless position on the reaction surface and of the Reynolds number (for $X = 2$ and $\alpha = 2$). This figure shows that for a low Reynolds number and an advanced position along the reaction surface, the diffusion boundary layer is thicker. This means that a long sensitive surface and low flow rate are real mass transport limitations for immunoassay applications.

Fig. 6 Average normalized complex concentration for the eight-experiment numbers
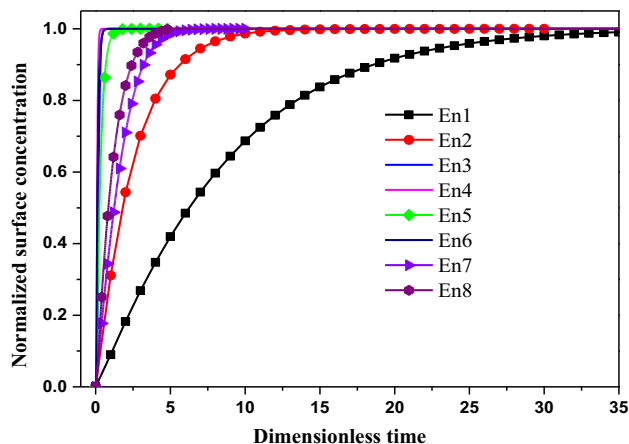
Table 4 Taguchi´s L8(2^7) orthogonal array and numerical results

Experiment number (En$_i$)	Response time: T_R^*	S/N ratio (dB)
1	23.57	− 2.7447
2	7.23	− 1.7183
3	0.37	0.8636
4	0.20	1.3979
5	0.86	0.131
6	0.33	0.96297
7	3.88	− 1.1777
8	3.02	− 0.96001

7.3 Taguchi optimization

Following the successful model validation, eight numerical simulations were performed using the combinations of design parameters in the specified orthogonal matrix table. Figure 6 illustrates the average normalized complex concentration in the reaction surface for all experiment number (En_i) of Table 3.

The response time of the microfluidic biosensor constitutes the main parameter of the analyte–ligand chemical kinetics. It corresponds to the time during which the concentration of the complex reaches its threshold value. Table 4 shows the numerical results for the response time and its S/N ratio of microfluidic biosensor using the experimental layout (Table 4).

In order to estimate the effect of the design parameters and to fix their relative importance on the reduction of the detection time of the device, an analysis of means and variance ANOVA was performed.

7.3.1 Analysis of means

The average value of the dimensionless detection times obtained can be calculated as (Eq. (8)):

$$\overline{T_R^*} = \frac{1}{8} \sum_{i=1}^{8} T_{Ri}^* = 4.93 \tag{8}$$

7.3.2 Calculation of mean effect

The mean value of response time of each factor is determined by (Eq. (9)):

$$Effect_{(F)} = 2 \frac{\sum Y^+ - \sum Y^-}{N} \tag{9}$$

Here, $N = 8$ is the total number of experiments, $Y^+ and Y^-$ terms are the responses when a given factor is at its high and low level, respectively. The average effects of all optimization factors for each level are shown in Table 5 and Fig. 7.

The minimum response time is obtained when all the optimization factors are at high level (Re$_2$, Da$_2$, σ$_2$, K$_{D2}$, Sc$_2$, α$_2$, X$_2$). This combination allows us to obtain a minimum detection time equal to 0.11.

Table 5 Mean value of response time for each level

Level	Re	Da	σ	K_D	Sc	α	X
1	7.843	7.998	9.425	7.170	6.823	6.913	6.995
2	2.025	1.868	0.44	2.695	3.043	2.953	2.87
Max–min	5.82	6.13	8.985	4.475	3.78	3.96	4.125
Rank	3	2	1	4	7	6	5

**Fig. 7** Main factor effects on response time
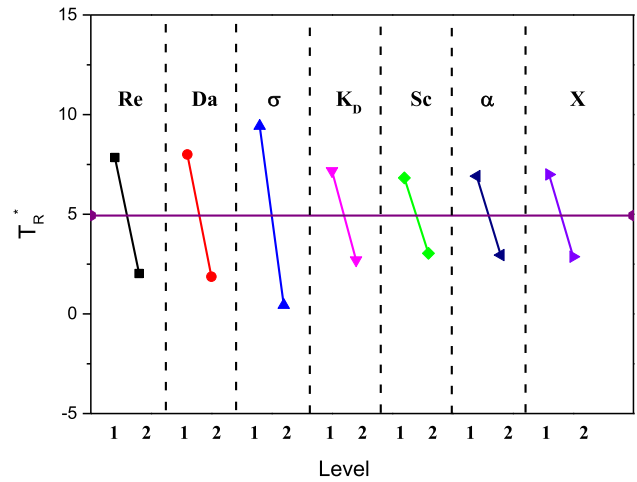
7.3.3 Analysis of variance

The effect of optimization factor in terms of signal-to-noise ratio (S/N) to reach minimum response of microfluidic biosensor is achieved based on lower the better criteria given by this equation [40, 41] (Eq. (10)):

$$S/N = -10\log_{10}\left(\frac{1}{n}\sum_{i=1}^{n} Y_i^2\right) \qquad (10)$$

Figure 8 illustrates the average effect of S/N ratio of response time for each factor. Table 6 presents the results of analysis of variance:

Fig. 8 Main effect of S/N ratio for response time
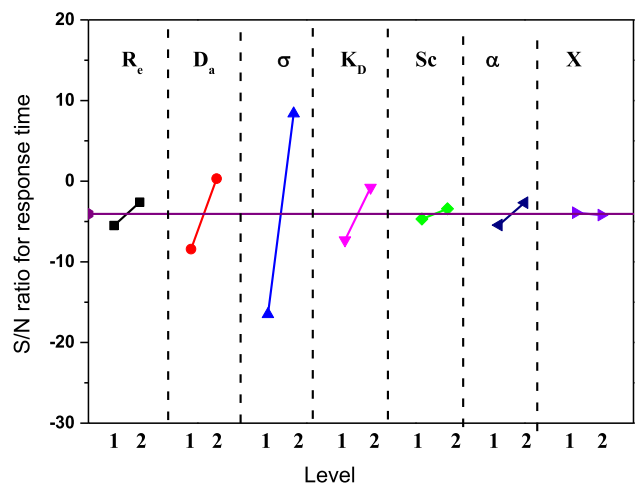
Table 6 Analysis of variance (ANOVA) for response time T_R^*

Symbol	Optimization parameter	D.f	Sum of squares	Mean square	Contribution %
Re	Reynolds number	1	67.745	67.745	15.45
Da	Damköhler number	1	75.154	75.154	17.14
σ	Relative adsorption capacity	1	161.46	161.46	36.83
K_D	Equilibrium constant	1	40.051	40.051	9.13
Sc	Schmidt number	1	28.577	28.577	6.51
α	Confinement coefficient	1	31.363	31.363	7.15
X	Confinement position	1	34.031	34.031	7.76
Error		0	0	–	–
Total		7	438.38		100

Fig. 9 Contribution of key parameters (Re, Da,, K_D, Sc, α and X) on the response time

The percentage contribution of each factor on the response time of the microfluidic biosensor is calculated by analysis of variance (Table 6). It is clear from Table 6 that the relative adsorption capacity (σ) has the highest contribution (36.83%), and the Schmidt number (Sc) has the lowest contribution (6.51%) to reduce the response time among the seven all factors. Further, the contribution of the Reynolds number (Re), Damköhler number (Da), equilibrium constant (K_D), confinement coefficient (α) and confinement position (X) to the minimization of response time is 15.45%, 17.14%, 9.13%, 7.15% and 7.76%, respectively. D.F is the degree of freedom (= number of level -1) (Fig. 9).

7.3.4 Multivariate regression analysis

Multivariate regression analysis is used to determine the relationship between the dependent variables of Reynolds number, Damköhler number, equilibrium constant, relative adsorption capacity, Schmidt number, confinement coefficient and confinement position. The dimensionless detection time T_R^* value obtained from the regression analysis of these key parameters is expressed by this equation (Eq. (11)):

$$T_R^* = 4.9 - 23.3Re - 24.5Da - 35.9\sigma - 17.9K_D - 15.1Sc - 15.8\alpha - 16.5X \tag{11}$$

The previous model is valid for $0.005 \leq Re \leq 0.01$, $5 \leq Da \leq 1000$, $0.02 \leq \sigma \leq 0.5$, $1 \leq K_D \leq 5, 10^4 \leq Sc \leq 10^5$, $0.1 \leq \alpha \leq 2$ and $0.5 \leq X \leq 2$. The sign of the coefficients of Eq. (11) indicates that all factors have a significant negative effect on T_R^*. That is, the increase in these factors contributes to the decrease the response time of microfluidic biosensor with flow confinement.

8 Conclusion

This study deals with the optimization of the design parameters of a microfluidic biosensor for the immunoassay of SARS-CoV-2. The detection is based on the efficiency of the reaction kinetics of the binding of SARS-Cov-2 under the effect of a few parameters.

This reaction takes place on a reaction surface, where ligands combine with analytes to create analyte–ligand complexes. A first-order adsorption model is proposed to govern this reaction. Analyte concentration is modeled by a stable distributed convection–diffusion equation in which the advection rate is assumed to satisfy the Navier–Stokes equation. Several numerical tests with critical parameters concerning Reynolds number (Re), Damköhler number (Da), relative adsorption capacity (σ), equilibrium dissociation constant (K_D), Schmidt number (Sc), confinement coefficient (α) and confinement position (X) with two levels are carried out. The new thing in this study is the use of the Taguchi method in the optimization analysis, and an L8(2^7) orthogonal table of seven critical parameters was designed. ANOVA methods are also employed to obtain the significance of each key parameter. The optimal combination of the key parameters obtained with current study is Re = 10^{-2}, Da = 1000, σ =0.5, K_D = 5, Sc 10^5, α = 2 and X = 2 to achieve the minimum dimensionless response time (0.11). The increase in these factors contributes to the decrease in the response time of microfluidic biosensor with flow confinement. It is expected that our investigation may provide new insights for future advancement in the design of microfluidic biosensor-based diagnostic devices for the detection, control, and prevention of COVID-19.

Data availability The data included in this manuscript are available and can be discussed (or shared), upon request to the corresponding author Sameh Kaziz.

References

1. H. Lu, C.W. Stratton, Y.W. Tang, Outbreak of pneumonia of unknown etiology in Wuhan, China: the mystery and the miracle. J. Med. Virol. **92**(4), 401 (2020)
2. E. Morales-Nárváez, C. Dincer, The impact of biosensing in a pandemic outbreak: COVID-19. Biosens. Bioelectron. **163**, 112274 (2020)
3. H. Zhu, Z. Fohlerová, J. Pekárek, E. Basova, P. Neužil, Recent advances in lab-on-a-chip technologies for viral diagnosis. Biosens. Bioelectron. **153**, 112041 (2020)
4. M. Sharifi et al., Cancer diagnosis using nanomaterials based electrochemical nanobiosensors. Biosens. Bioelectron. **126**, 773–784 (2019)
5. M. Sharifi et al., Plasmonic and chiroplasmonic nanobiosensors based on gold nanoparticles. Talanta **212**, 120782 (2020)
6. V.M. Corman et al., Detection of 2019 novel coronavirus (2019-nCoV) by real-time RT-PCR. Eurosurveillance **25**(3), 2000045 (2020)
7. J.-L. He et al., Diagnostic performance between CT and initial real-time RT-PCR for clinically suspected 2019 coronavirus disease (COVID-19) patients outside Wuhan, China. Respir. Med. **168**, 105980 (2020)
8. C.T. Pachucki, M.A. Khurshid, J. Nawrocki, Utility of reverse transcriptase PCR for rapid diagnosis of influenza a virus infection and detection of amantadine-resistant influenza a virus isolates. J. Clin. Microbiol. **42**(6), 2796–2798 (2004)
9. S.V. Vemula, J. Zhao, J. Liu, X. Wang, S. Biswas, I. Hewlett, Current approaches for diagnosis of influenza virus infections in humans. Viruses **8**(4), 96 (2016)
10. J.R. Choi, Development of point-of-care biosensors for COVID-19. Front. Chem. **8**, 517 (2020)
11. C. Sheridan, Fast, portable tests come online to curb coronavirus pandemic. Nat Biotechnol **38**(5), 515–518 (2020)
12. J. Zhifeng, A. Feng, T. Li, Consistency analysis of COVID-19 nucleic acid tests and the changes of lung CT. J. Clin. Virol. **127**, 104359 (2020)
13. R. Tang et al., A fully disposable and integrated paper-based device for nucleic acid extraction, amplification and detection. Lab. Chip. **17**(7), 1270–1279 (2017)
14. Y. Saad, M. Selmi, M.H. Gazzah, H. Belmabrouk, The magnetic field effect on the improvement of the binding reaction of C-reactive protein at the microfluidic channel surface of an SPR biosensor. Eur Phys J Plus **136**(5), 1–17 (2021)
15. F. Echouchene, T. Al-shahrani, H. Belmabrouk, Enhancement of heterogeneous microfluidic immunosensors using new sensing area shape with electrothermal effect. Appl. Sci. **11**(10), 4566 (2021)
16. S. Kaziz, I. Ben Mariem, F. Echouchene, M.H. Gazzah, H. Belmabrouk, Design parameters optimization of an electrothermal flow biosensor for the SARS-CoV-2 S protein immunoassay. Indian J Phys (2022). https://doi.org/10.1007/s12648-022-02360-w
17. S. Kaziz, Y. Saad, M. Bouzid, M. Selmi, H. Belmabrouk, Enhancement of COVID-19 detection time by means of electrothermal force. Microfluid. Nanofluid. **25**(10), 1–12 (2021)
18. S. Kaziz, Y. Saad, M.H. Gazzah, H. Belmabrouk, 3D simulation of microfluidic biosensor for SARS-CoV-2 S protein binding kinetics using new reaction surface design. Eur. Phys. J. Plus **137**(2), 1–12 (2022)
19. G.U. Lee, S. Metzger, M. Natesan, C. Yanavich, Y.F. Dufrêne, Implementation of force differentiation in the immunoassay. Anal. Biochem. **287**(2), 261–271 (2000)
20. M. Selmi, F. Echouchene, M.H. Gazzah, H. Belmabrouk, Flow confinement enhancement of heterogeneous immunoassays in microfluidics. IEEE Sens. J. **15**(12), 7321–7328 (2015)
21. M. Selmi, M.H. Gazzah, H. Belmabrouk, Optimization of microfluidic biosensor efficiency by means of fluid flow engineering. Sci. Rep. **7**(1), 1–11 (2017)
22. F. Shahbazi, M. Jabbari, M.N. Esfahani, A. Keshmiri, A computational simulation platform for designing real-time monitoring systems with application to COVID-19. Biosens. Bioelectron. **171**, 112716 (2021)
23. P. D. Berger, R. E. Maurer, and G. B. Celli, "Experimental design," *CA (USA): Wadsworth Group Belmont,* 2002.
24. M. Pillet, *Les plans d'expériences par la méthode Taguchi*. Maurice Pillet, 2001.
25. C.-H. Wu, W.-S. Chen, Injection molding and injection compression molding of three-beam grating of DVD pickup lens. Sens. Actuators, A **125**(2), 367–375 (2006)
26. E.Y. Ng, W.K. Ng, Parametric study of the biopotential equation for breast tumour identification using ANOVA and Taguchi method. Med. Biol. Eng. Compu. **44**(1), 131–139 (2006)
27. N. Daneshvar, A. Khataee, M. Rasoulifard, M. Pourhassan, Biodegradation of dye solution containing malachite green: optimization of effective parameters using Taguchi method. J. Hazard. Mater. **143**(1–2), 214–219 (2007)
28. B.J. du Plessis, G. De Villiers, The application of the Taguchi method in the evaluation of mechanical flotation in waste activated sludge thickening. Resour. Conserv. Recycl. **50**(2), 202–210 (2007)
29. J.-Y. Houng, J.-H. Liao, J.-Y. Wu, S.-C. Shen, H.-F. Hsu, Enhancement of asymmetric bioreduction of ethyl 4-chloro acetoacetate by the design of composition of culture medium and reaction conditions. Process Biochem. **42**(1), 1–7 (2007)

30. R. Romero-Villafranca, L. Zúnica, R. Romero-Zúnica, Ds-optimal experimental plans for robust parameter design. J. Stat. Plan. Inference **137**(4), 1488–1495 (2007)

31. M. R. Dahman, "AMSM-Analysis Of Variance (ANOVA)-Chapter Nine," 2018.

32. J.A. Thompson, H.H. Bau, Microfluidic, bead-based assay: theory and experiments. J. Chromatogr. B **878**(2), 228–236 (2010)

33. O. Hofmann, G. Voirin, P. Niedermann, A. Manz, Three-dimensional microfluidic confinement for efficient sample delivery to biosensor surfaces. Application to immunoassays on planar optical waveguides. Anal. Chem. **74**(20), 5243–5250 (2002)

34. M. Zimmermann, E. Delamarche, M. Wolf, P. Hunziker, Modeling and optimization of high-sensitivity, low-volume microfluidic-based surface immunoassays. Biomed. Microdevice **7**(2), 99–110 (2005)

35. T. Gervais, K.F. Jensen, Mass transport and surface reactions in microfluidic systems. Chem. Eng. Sci. **61**(4), 1102–1121 (2006)

36. S. Jomeh, M. Hoorfar, Numerical modeling of mass transport in microfluidic biomolecule-capturing devices equipped with reactive surfaces. Chem. Eng. J. **165**(2), 668–677 (2010)

37. Z. Chen, *The finite element method: its fundamentals and applications in engineering* (World Scientific, 2011)

38. I. Chaiken, S. Rosé, R. Karlsson, Analysis of macromolecular interactions using immobilized ligands. Anal. Biochem. **201**(2), 197–210 (1992)

39. M.J. Eddowes, *"Theoretical methods for analysing biosensor performance," biosensors: a practical approach* (IRL Press, Oxford University Press, Oxford, 1990), pp.211–263

40. A. Bagchi, S. Saravanan, G.S. Kumar, G. Murugan, K. Raghukandan, Numerical simulation and optimization in pulsed Nd: YAG laser welding of Hastelloy C-276 through Taguchi method and artificial neural network. Optik **146**, 80–89 (2017)

41. J.-H. Sun, Y.-C. Fang, B.-R. Hsueh, Combining Taguchi with fuzzy method on extended optimal design of miniature zoom optics with liquid lens. Optik **123**(19), 1768–1774 (2012)